

This is the **accepted version** of the article:

Robbennolt, Shauna; Nicolenco, Aliona; Mercier Fernández, Pau; [et al.]. «Electric field control of magnetism in iron oxide nanoporous thin film». ACS Applied Materials and Interfaces, Vol. 11, issue 40 (Oct. 2019), p. 37338-37346. DOI 10.1021/acsami.9b13483

This version is available at <https://ddd.uab.cat/record/221642>

under the terms of the  **CC BY** license

Electric Field Control of Magnetism in Iron Oxide Nanoporous Thin Films

Shauna Robbennolt,^{1,a} Aliona Nicolenco,^{1,2} Pau Mercier Fernandez,¹ Stéphane Auffret,³

Vincent Baltz,³ Eva Pellicer,¹ Enric Menéndez,¹ Jordi Sort^{1,4,b}

¹ *Departament de Física, Universitat Autònoma de Barcelona, E-08193 Bellaterra (Cerdanyola del Vallès), Spain*

² *Institute of Applied Physics, MD – 2028 Chisinau, Moldova*

³ *SPINTEC, Univ. Grenoble Alpes/CNRS/INAC-CEA, F-38000 Grenoble, France*

⁴ *Institució Catalana de Recerca i Estudis Avançats (ICREA), Pg. Lluís Companys 23, E-08010 Barcelona, Spain*

Corresponding Author

^a Shauna Robbennolt – shaunaaryn.robbennolt@uab.cat

^b Jordi Sort – jordi.sort@uab.cat

ABSTRACT

Voltage control of the magnetic properties of oxide thin films is highly appealing to enhance energy efficiency in miniaturized spintronic and magnetoelectric devices. Herein, magnetoelectric effects in electrolyte-gated nanoporous iron oxide films are investigated. Highly porous films were prepared by the evaporation-induced self-assembly of sol-gel precursors with a sacrificial block copolymer template. For comparison, films with less porosity but analogous crystallographic structure were also prepared using an identical procedure except without the polymer template. The templated (highly porous) films showed a very large magnetoelectric response with a maximum increase in magnetic moment at saturation of a factor of 13 and a noticeable (two-fold) increase of coercivity (after applying – 50 V). The non-templated films also exhibited a pronounced increase of magnetic moment at saturation of a factor of 4, although the coercivity remained unaffected over the same voltage range. Magnetoelectric effects in these latter films were found to be fully reversible in the

voltage window ± 10 V. The observed changes in magnetic properties are concluded to be magneto-ionically driven with oxygen ion exchange between the iron oxide and the liquid electrolyte, as evidenced from Raman and X-ray photoelectron spectroscopy experiments.

Keywords: magnetoelectric, nanoporous thin films, iron oxide, oxygen migration.

INTRODUCTION

Magnetic materials are widely utilized in diverse applications ranging from data storage systems¹⁻⁸ to biomedical devices.⁹⁻¹⁶ Conventionally, magnetic materials are manipulated with external magnetic fields generated using electromagnets (*i.e.*, by passing electric currents through a conducting wire). This causes power dissipation due to resistive heating. These Joule heating effects are particularly noticeable as devices are progressively shrunk in size. Thus, the conventional way to control the magnetic response of materials in miniaturized systems is energetically rather costly. This has spurred a significant research effort to tune magnetism in nano- and micro-scale magnetic materials directly with voltage, with lower (or even without) associated flowing electric currents.¹⁷⁻²⁸

There are a number of magnetoelectric coupling mechanisms that are currently being exploited to electrically tune the magnetic properties of materials, either using solid or liquid electrolytes.^{18,29,30} Of particular interest is the relatively new field of magneto-ionics in which ionic migration (of, *e.g.*, oxygen anions) is used to tailor the saturation magnetization (M_S), coercivity (H_C), magnetic anisotropy direction and other properties of these materials.^{24,31-38} In metal oxides, magnetism arises from unpaired d -electrons in the transition metal atoms which (by convention) can either be spin up or spin down. If the magnetic moments on each cation are all equivalent and anti-parallel aligned, the material is antiferromagnetic and the sample has no measurable magnetic moment. However, if some cations have a higher magnetic moment than others, the sample then has an overall magnetic moment due to the uncompensated spins in one direction, resulting in ferrimagnetic behavior. The number of unpaired spins on a given cation is a function of the metal, its oxidation state and the type of crystallographic site in which it is located (*e.g.*, octahedral *versus* tetrahedral sites). Importantly, the oxidation state of a cation and, to a lesser degree, the crystallographic site occupancies can be controlled by oxygen ion migration. For example, if a negative electric

field is applied to a metal oxide magnet and oxygen is driven out of the material, the total number of anions decreases and, concomitantly, the number of cations must be reduced as well (*i.e.*, the average oxidation state decreased) to compensate the loss of negative charges. Likewise, if a positive electric field is applied, oxygen can be driven into the sample (if it is available) and the average oxidation state of the cations must then increase to compensate electric charges. Hence, by changing the oxidation state of the cations, their magnetic moments and the degree to which they are cancelled out antiferromagnetically can be both manipulated.

Among the various types of materials where magnetoelectric effects have been investigated, porous alloys and oxides have gained considerable attention because (i) they allow for large electric surface charge accumulation (in metals, electric field is screened at their outer surface, within Thomas-Fermi screening length)^{18,30} and (ii) they exhibit a very high surface area which allows for enhanced electric-field control of the magnetic properties, both by magneto-ionic means³⁹⁻⁴¹ (in case the pores are filled with liquid electrolytes that promote ion intercalation or redox reactions) and other magnetoelectric coupling mechanisms.^{27,42-45} Moreover, in a porous material, the effective thickness of the magnetic material is limited by the thickness of the ligaments which allows for the fabrication of materials that maintain favorable, nanoscale properties at the micro-scale and bulk scale.

Ion intercalation and redox reactions in oxide materials have been intensively investigated in recent years as an energy-efficient way to tailor their magnetic properties.^{29,30} Among diverse existing magnetic oxides, iron oxide is one of the most appealing because it is cheap, earth-abundant, non-toxic and there are a number of types of iron oxide (*e.g.*, antiferromagnetic hematite [α -Fe₂O₃], ferrimagnetic maghemite [γ -Fe₂O₃] or ferrimagnetic magnetite [Fe₃O₄]) each of which with unique magnetic properties.⁴⁶⁻⁴⁹ There are just a few reports of magneto-ionic manipulation in iron/iron oxide systems. Duschek *et al.* fabricated nanoislands of Fe that were then reversibly oxidized and re-reduced between Fe and FeO_x,

electrochemically, in a KOH solution.³⁷ They found that the smaller islands with thicknesses of only several nanometers performed the best and that, overall, the nanoisland-based films showed an enhanced magnetoelectric response compared to continuous films, highlighting the importance of the nanoscale structure in magneto-ionically manipulated systems. The same group also investigated magneto-ionic control of magnetism in Fe thin films grown on top of FePt and were able to control the magnetic anisotropy of the films by partially oxidizing the Fe, thereby effectively changing the thickness of the Fe layer.⁵⁰ In addition to these works, there are reports on magnetoelectric manipulation of iron oxides by other means. Namely, Dasgupta *et al.* and Zhang *et al.* used Li⁺ intercalation to change the magnetic properties of nanocrystalline maghemite (γ -Fe₂O₃).^{25,51} Maghemite is a spinel crystal structure, similar to magnetite (Fe₃O₄) except that in maghemite almost all of the Fe atoms are Fe³⁺ and the extra cationic charge is balanced by cation vacancies. Dasgupta *et al.* found that, initially, Li⁺ intercalation reduced Fe³⁺ in tetrahedral vacancies to Fe²⁺ ions, which then migrated into unoccupied octahedral sites leading to a small increase in magnetization. In a second stage, direct reduction of octahedral Fe³⁺ to Fe²⁺ dominated the change in the magnetic properties, causing a significant decrease in the sample's magnetic moment. The studies by Zhang *et al.* revealed that a fully reversible transition from α -Fe₂O₃ to metallic Fe due to Li⁺ incorporation could take place for sufficiently small α -Fe₂O₃ particles. In turn, Traußnig *et al.* demonstrated magnetoelectric control via surface charging in a nanocomposite comprising maghemite and Pt nanoparticles. Charge accumulation alters the magnetic properties of materials by changing the *d*-orbital occupancy near the surface.⁵² Since the effect is surface-based, it is typically observed in ultra-thin films, but in the case of Traußnig *et al.*, the Pt nanoparticles carried the surface charge into the material, hence allowing thicker samples to be affected. In another work, Gich *et al.* demonstrated that ϵ -Fe₂O₃, a rare phase of iron oxide, is multiferroic at room temperature, meaning that an applied electric field can directly change the resulting magnetic

properties.^{48,53} More recently, magneto-ionic spin dynamics modulation in Fe₃O₄ thin films⁵⁴ and non-volatile electric control of exchange bias by a redox reaction in FeO_x/Fe/IrMn systems⁵⁵ have been demonstrated.

In this work, we investigate the impact of porosity on the magneto-ionic manipulation of magnetism in iron oxide thin films. The films are synthesized using sol-gel and dip-coating methods. To fabricate highly porous films, we employ a technique called block copolymer templating where a micelle-forming, di-block copolymer is added to the solution. The polymer and sol-gel precursors undergo evaporation induced self-assembly (EISA) during the dip-coating process and, then, films are heated to crystallize the iron oxide and remove the polymer template, leaving behind the porous structure. In the absence of the polymer template, solvent evaporation alone also induces some degree of porosity. An electrochemical cell is used to apply electric fields *in situ* (*i.e.*, while the magnetic properties of the films are being measured). The magnetoelectric responses of templated and non-templated iron oxide films are compared and the former exhibits much larger effects. Interpretation of the results is performed using Raman and X-ray photoelectron spectroscopy (XPS) experiments, from which the magneto-ionic origin (*i.e.*, oxygen ion migration) of the observed effects is inferred.

MATERIALS AND METHODS

Materials. Iron(II) chloride tetrahydrate (99.999%), citric acid and propylene carbonate (*PC*) were purchased from Sigma-Aldrich. Poly(butadiene oxide)-*b*-Poly(ethylene oxide) with M_n: PBd(5600)-*b*-EO(10000), was obtained from Polymer Source. Platinum wire (99.9%) for the counter electrode was purchased from Alfa Aesar. All chemicals were used without further purification.

Preparation of the Sol-Gel Solutions. The sol-gel solution was prepared following a previously published recipe. 400 mg of FeCl₂·4H₂O and 380 mg of citric acid were dissolved

in 10 mL of ethanol and the resulting mixture was stirred overnight yielding an orange/green, clear solution. Simultaneously, 30 mg of PBd-b-EO was dissolved in 5 mL of ethanol and allowed to stir overnight. The next day, half of the solution containing the dissolved iron salt (5 mL) was added to the dissolved polymer and 5 mL of ethanol was added to the remaining half to ensure the concentrations were equal. The solution without the polymer was used to make the non-templated films while the one with polymer was used to make the more porous, templated films.

Thin Film Deposition. The substrates were prepared by sputtering 70 nm of Pt onto wafers of [100]-oriented Si which were then cut into 3×1 cm² chips. The solution was deposited by dip-coating with a withdrawal rate of 300 mm/min using a Coater 5 AC from id Lab. The films were immediately transferred to a hot-plate at 80 °C to aid the evaporation of the solvent before being heated in air to 600 °C at a rate of 3 °C/min. They were then held at 600 °C for 3 h before being allowed to cool to room temperature. The non-templated and templated films were prepared simultaneously, and the films were all found to be 75-85 nm thick.

Magnetic Characterization. A MicroSense (LOT-QuantumDesign) Vibrating Sample Magnetometer (VSM) was used to measure the magnetic properties. The voltage was applied *in situ* using an Agilent B2902A power supply and a small electrochemical cell attached to a VSM sample holder, as described in detail in our previous works.³⁸⁻⁴⁰ Briefly, the sample was the working electrode and contact was made to the Pt layer under the iron oxide. A Pt wire was used as the counter electrode and was placed along with the sample in a small Eppendorf tube (1 mL). The electrolyte solution was propylene carbonate treated with metallic sodium to remove any traces of water. The sodium treatment left a small amount of Na⁺ and OH⁻ ions (≈ 5 ppm Na⁺ as determined by Inductively Coupled Plasma Spectroscopy) and no other salts were added. All magnetic measurements were taken in an in-plane configuration at room temperature and the indicated voltages were each applied for 40 min (unless otherwise stated)

following this sequence: 0 V, -10 V, -20 V, -30 V, -40 V, -50 V, 0 V, +10 V, +20 V, +30 V, +40 V, +50 V.

Structural and Elemental Characterization. Field Emission Scanning Electron Microscope (FE-SEM, Zeiss Merlin) was used to characterize the microstructure of the films. XPS analyses on the film surface were performed using a PHI 5500 Multitechnique System (Physical Electronics) with a monochromatic Al K_{α} source under ultra-high vacuum. The spectra were calibrated using the carbon peak that arises from “adventitious” carbon on the film after exposure to air. The XPS measurements were necessarily performed *ex situ* by placing the sample into an electrochemical cell (identical to that described above for the magnetic characterization) for the application of voltage (40 min). The samples were then removed, immediately placed in the XPS chamber under ultra-high vacuum and the measurements were performed. The Raman spectra were also collected *ex situ* using a Jobin-Yvon LabRam HR 800 equipped with an Olympus BXFM optical microscope. The laser was 532 nm, the power was set to 4 mW, 50x objective was used and detector was a CCD kept at -70°C .

RESULTS AND DISCUSSION

Figure 1 shows top-view scanning electron microscopy (SEM) images of the non-templated (**a,b**) and templated porous (**c,d**) films at medium (**a,c**) and high (**b,d**) magnifications. It is clear from these images that the non-templated film exhibits already some porosity, which likely results from solvent evaporation channels forming during the heat treatments. The templated film clearly shows higher porosity, as it could be anticipated. The pores in the templated film appear larger and mostly with rounded shape, which is expected since the polymer template used is known to form spherical micelles in ethanol. On the other hand, the pores in the non-templated film are smaller and comprise a mixture of round/oblong

and crack-like geometries, which is consistent with porosity induced during rapid solvent evaporation.

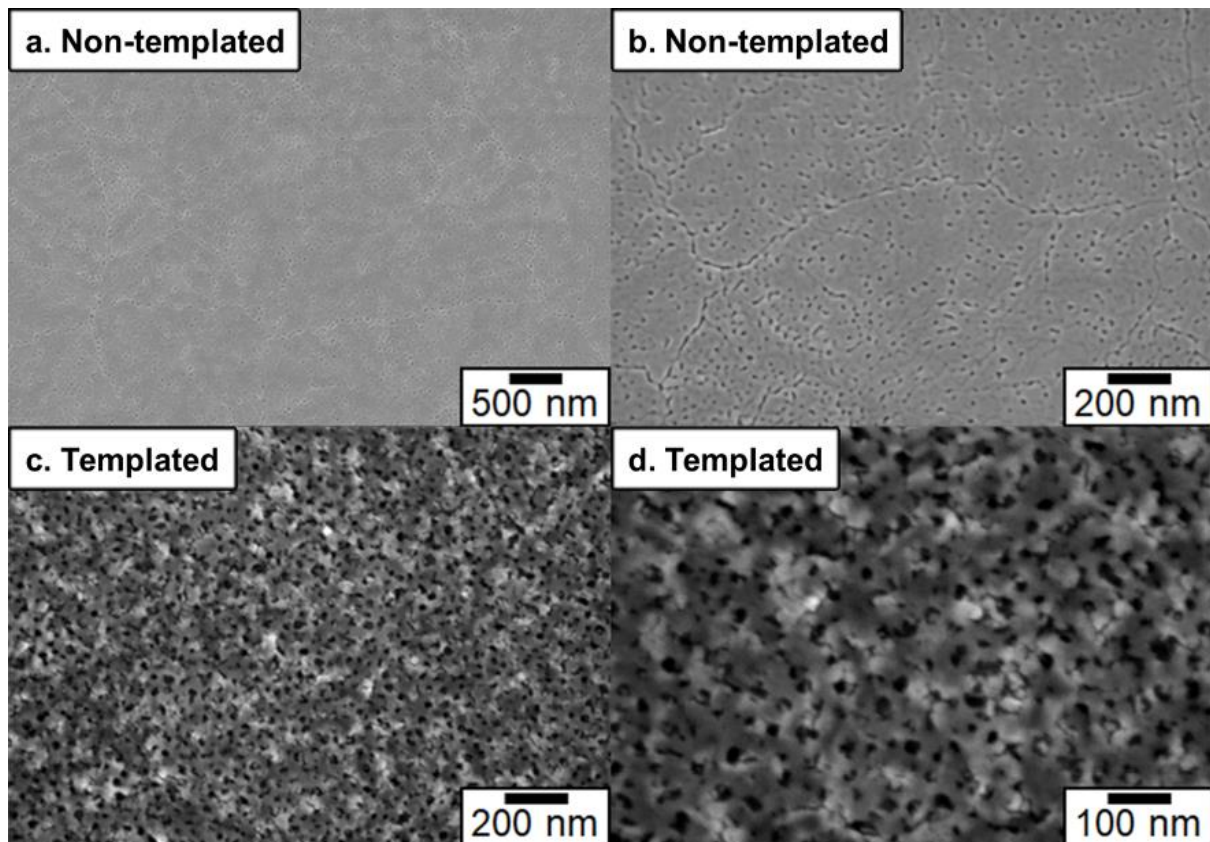


Figure 1. Top-view SEM images of a non-templated film at (a) low and (b) high magnifications and a templated film at (c) low and (d) high magnifications.

The magnetoelectric properties of the films were investigated by recording the magnetic moment m vs. the applied magnetic field (i.e., m - H_{applied}) loops as a function of applied voltage (*in situ*, using the propylene carbonate electrolyte). It is important to highlight that, in this material system, it is very difficult to mass normalize the magnetic moment because techniques such as Inductively Coupled Plasma Spectroscopy (ICP) are not sensitive to the oxygen content. It is also difficult to obtain the magnetization (magnetic moment per unit volume) due to the porosity. Therefore, in this work, the magnetic moment is normalized such that the magnetic moment at saturation of the initial state of the sample is set to 1. Each hysteresis loop was consecutively acquired on a single sample that was not moved between measurements, so that the relative voltage-induced changes are indeed quantifiable (and discussed here as relative

percentages). **Figure 2** shows the hysteresis loops for the non-templated films. **Figure 2a** shows the hysteresis loop of the sample in the initial state (black line) and as a function of voltage from -10 V (purple line) to -50 V (red line). The m_S increases by 395% from the initial state to after -50 V. The coercivity (H_C) is found to remain at 88 Oe over the same voltage range.

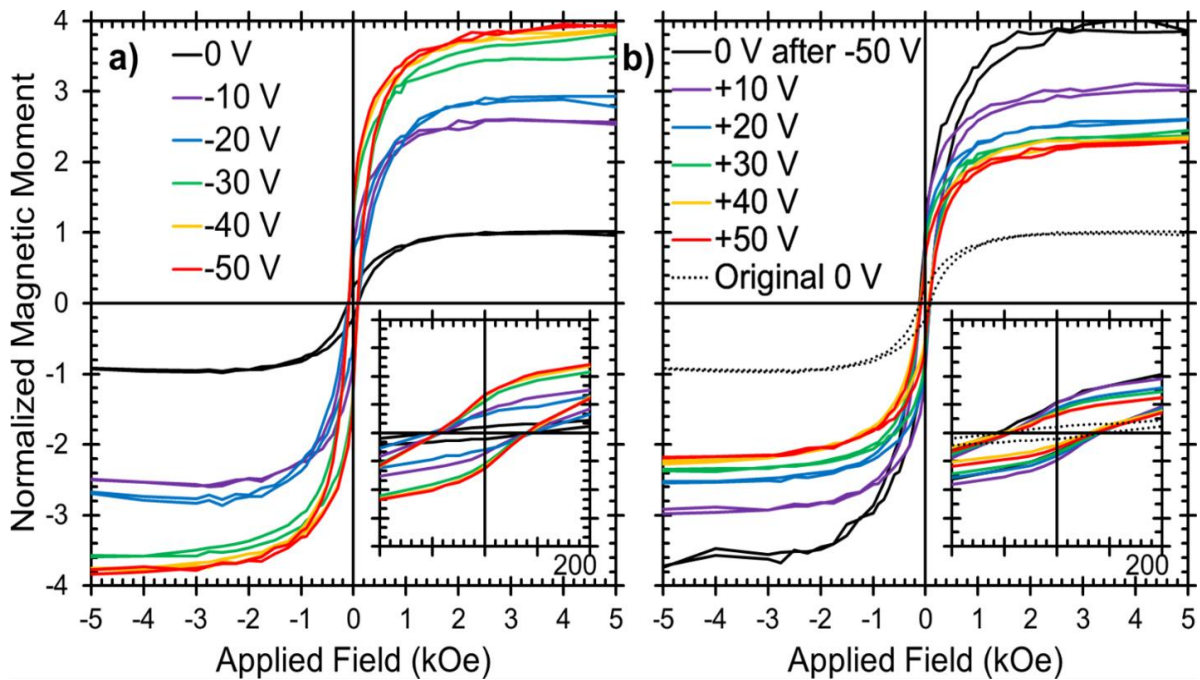


Figure 2. Room-temperature magnetic hysteresis loops of a non-templated film as a function of applied voltage. Negative voltages were applied first (a), followed by positive voltages (b). The loops are normalized such that the magnetic moment at saturation of the initial state is set to 1.

After applying -50 V, the voltage was returned to 0 V for 40 min and **Figure 2b** shows the same sample (unmoved) going from that 0 V state (black line) to $+50$ V (red line). There is no appreciable change in the hysteresis loop taken under -50 V and the loop taken afterwards at 0 V which demonstrates the non-volatility of the magnetic changes induced here. Upon the application of positive voltage, the magnetic moment at saturation decreases by 58% between 0 V and $+50$ V. The initial state is shown in a black dotted line for comparison (same as the black solid line in **Figure 2a**). The change in magnetic moment at saturation between $+30$ V and $+50$ V is very small, which suggests that the system is reaching a limit. This limit is well

above the initial sample state which means that the changes induced at -50 V are only partially reversible.

The same experiments were performed on templated, highly porous, films and the results are presented in **Figure 3**. The hysteresis loop of the sample in the initial state is shown in black in **Figure 3a**. Compared to the non-templated film, the H_C is higher (160 Oe vs. 88 Oe for the non-templated film) which is consistent with previous reports of porous films fabricated using block-copolymer templating of sol-gel precursors and is likely due to the pores limiting domain wall propagation.⁵⁶ As noted above, the M_S between the two films is not comparable since the magnetic moment could not be accurately normalized. The hysteresis loops as a function of voltage from -10 V (purple line) to -50 V (red line) are shown in **Figure 3a**. Here, the magnetic moment at saturation increases by 1310% from the initial state to the loop after application of -50 V. The coercivity also increases in this case, up to 320 Oe. The relative change in M_S is more than three times higher than the relative change seen in the non-templated film shown in **Figure 2**. This demonstrates the importance of porosity in facilitating the magnetic changes observed here.

Contrary to the non-templated film, the hysteresis loop at -50 V (**Figure 3a**) and the loop taken at 0 V afterwards (**Figure 3b**) are dissimilar in the case of the templated film. The magnetic moment at saturation is found to be 18% smaller at 0 V (after the removal of -50 V) than it was at -50 V. The magnetic moment at saturation then further decreases by 32% between the same 0 V and the application of $+50$ V. Again, the hysteresis loop of the initial state is shown in **Figure 3b** in black dotted lines for comparison. These results indicate that, similar to the non-templated film, the induced changes in magnetic properties are only partially reversible after $+50$ V (the magnetic moment at saturation remains higher than it was in the initial state).

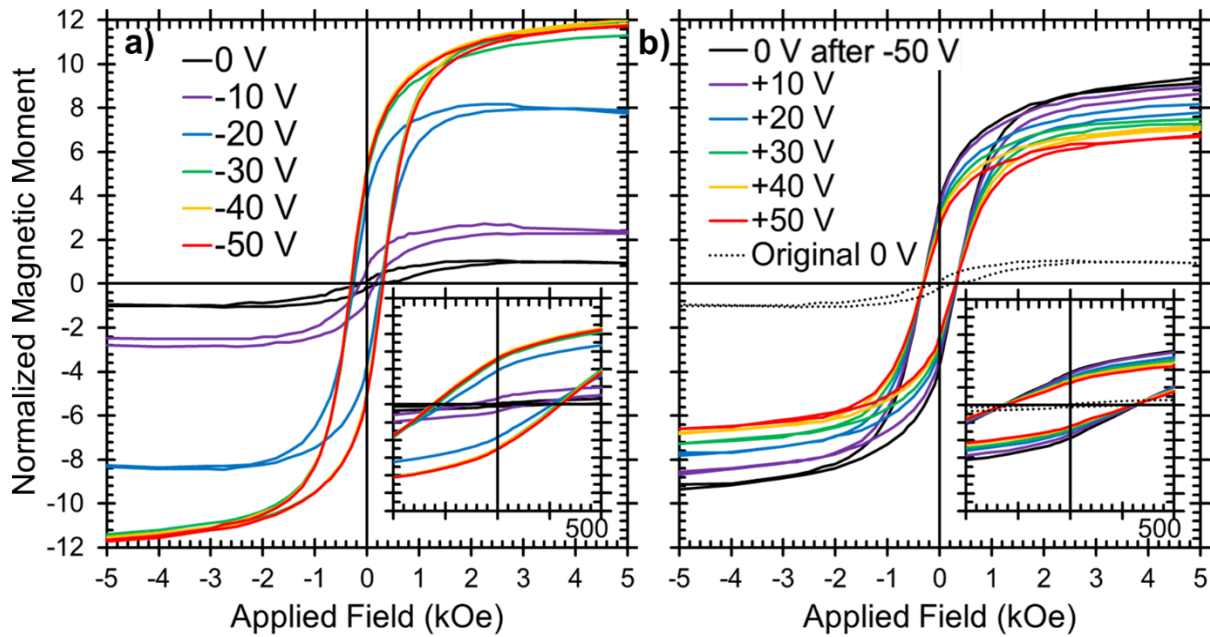


Figure 3. Room-temperature magnetic hysteresis loops of a templated film as a function of applied voltage. Negative voltages were applied first (a), followed by positive voltages (b). As with the non-templated films, the loops are normalized such that the saturation magnetization of the initial state is set to 1.

It is interesting to note that the progression of the changes in magnetic moment at saturation as a function of voltage is very different between the non-templated and templated samples. This is most clearly seen during the application of positive voltages. In the non-templated sample (**Figure 2b**), the application of +10 V leads to a significant decrease in magnetic moment at saturation but the incremental decrease in magnetic moment at saturation for each additional 10 V gets rapidly smaller. In contrast, the decrease in magnetic moment at saturation in the templated film (**Figure 3b**) is rather constant between each 10 V increment. The opposite trend is seen, although less clearly, when negative voltages are applied. In the templated sample (**Figure 3a**), the M_S increases dramatically for -10 V and -20 V, but seems to reach a limit below -30 V. The non-templated sample (**Figure 2a**) also shows a dramatic increase in M_S for -10 V, but the incremental changes following are more regular than in the templated film. These differences again serve to highlight the importance of porosity in these systems.

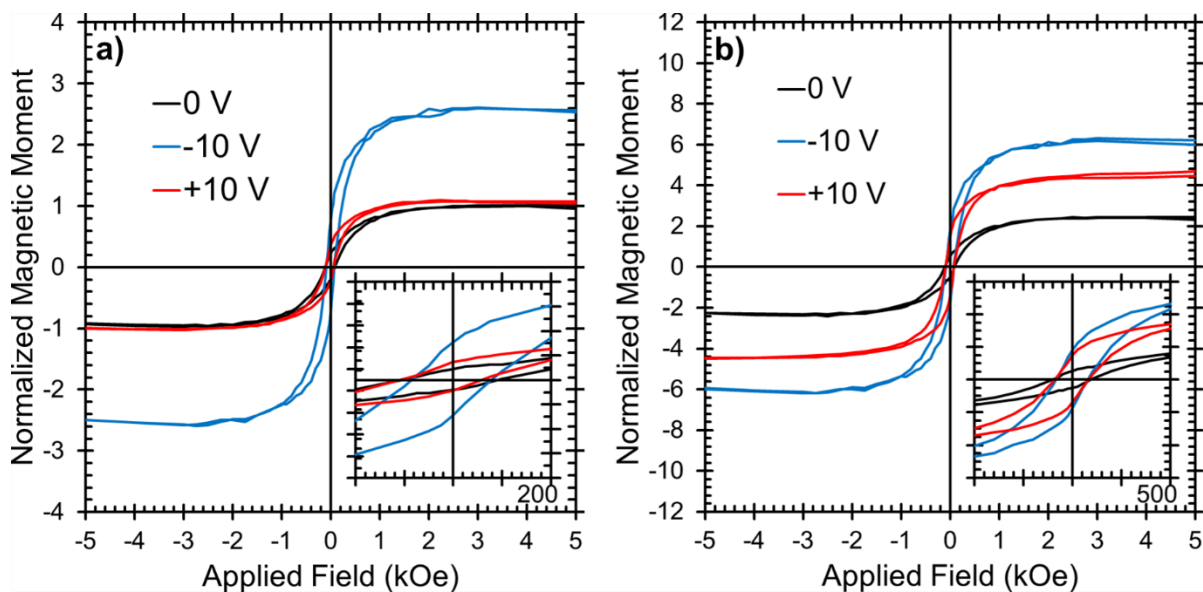


Figure 4. Room-temperature magnetic hysteresis loops of a non-templated **(a)** and templated **(b)** film as a function of applied voltage showing the system reversibility. The loops are normalized such that the saturation magnetization of the initial state is set to 1.

We further investigated the reversibility of the observed magnetoelectric effect using identical FeO_x films and a smaller potential window (± 10 V). The results obtained for the non-templated film are presented in **Figure 4a**. It is worth noting that the change in magnetic moment at saturation observed between 0 V and -10 V was the same (160% increase), as it is shown in **Figure 2a,b**. We found that the changes induced by -10 V were entirely reversible with the application of $+10$ V, which can be advantageous for device applications such as magnetic data storage where re-writability is important. In the templated film the changes induced by -10 V were not entirely reversible at $+10$ V, as shown in **Figure 4b**. This suggests that the additional porosity brought by block-copolymer templating resulted in larger charges in magnetic moment at saturation (1310% vs. 395% for the non-templated film), but the non-templated film performs better in terms of reversibility.

Based on previous works, it could be expected that these magnetoelectric changes proceed primarily through a magneto-ionic mechanism.^{39–41} To test this hypothesis, XPS experiments were performed. The resulting spectra are presented in **Figure 5**. It is important

to note that because XPS requires of ultra-high vacuum, the measurements had to be performed *ex situ*. Spectra were taken in the initial state, after the application of -10 V and then after the application of $+10$ V (i.e., the voltage window where the full reversibility was obtained in non-templated FeO_x). Voltage was applied using the same electrochemical cell described above, for 40 min, and then the sample was rinsed with ethanol, air dried and then loaded into the vacuum chamber. The spectra were fit, and the peaks corresponding to the different iron oxidation states are shown with different colors. The peaks were identified based on previous assignments found in the NIST XPS

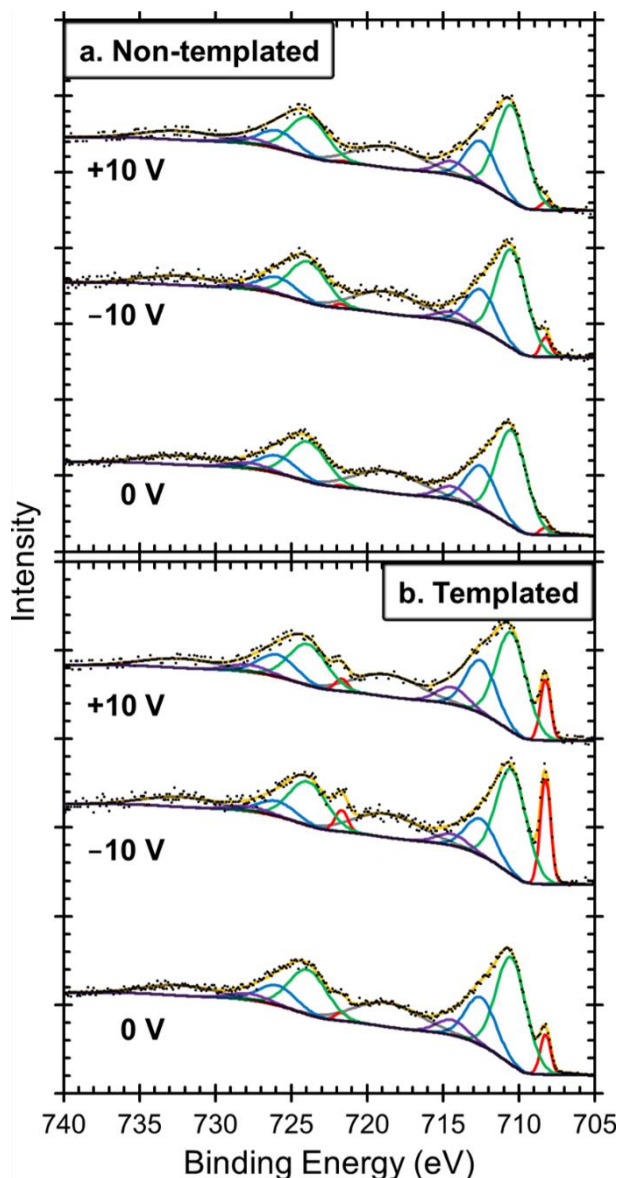


Figure 5. XPS spectra of (a) the non-templated and (b) templated FeO_x films in the initial state, after -10 V and after $+10$ V. The peak fits are shown: the blue line belongs to Fe^{3+} contribution, the green line to Fe^{2+} , and the red to Fe^0 . Purple line shows the satellite peaks.

in purple are satellite peaks. Looking first at the non-templated film (**Figure 5a**), in the initial state, the iron is 30.1% Fe^{3+} , 67.9% Fe^{2+} and 1.9% Fe^0 . After the application of -10 V, the sample is reduced and the Fe^{3+} content decreases to 27.8%, Fe^{2+} stays almost the same at 67.5% and the Fe^0 increases to 4.7% (**Table 1**). This is consistent with oxygen migration across the iron oxide film and out of the sample, either to the local pore surface, or stabilized in the solution.⁵⁹ Upon application of $+10$ V, the sample largely recovers, consistent with oxygen migration back into the sample. The Fe^{3+} content increases back to 30.2%, Fe^{2+} remains at

67.8% and, the Fe⁰ decreases back to 2.0%. These results are consistent with the magnetic data shown in **Figure 4a**. Namely, after the application of –10 V, the reduction of the Fe corresponds to an increase in magnetic moment at saturation and then, after the application of +10 V, the Fe is completely re-oxidized, and the magnetic moment at saturation returns close to its initial value.

Table 1. The percentage of each Fe state determined by calculating the area of the corresponding XPS peaks.

Applied voltage	Fe states in <i>non-templated</i> FeO _x			Fe states in <i>templated</i> FeO _x		
	Fe ³⁺ ,%	Fe ²⁺ ,%	Fe ⁰ ,%	Fe ³⁺ ,%	Fe ²⁺ ,%	Fe ⁰ ,%
0 V	30.1	67.9	1.9	28.4	64.0	8.2
–10 V	27.8	67.5	4.7	20.4	59.1	20.4
+10 V	30.2	67.8	2.0	30.6	57.1	12.1

In the pristine templated sample (**Figure 5b**), iron is initially consisting of 28.4 % Fe³⁺, 64.0% Fe²⁺ and 8.2% Fe⁰ states. After the application of –10 V, the Fe³⁺ content decreases to 20.4%, Fe²⁺ decreases to 59.1% and 20.4% is found to be Fe⁰. Then, after the application of +10 V, the Fe³⁺ content increases to 30.6%, Fe²⁺ decreases to 57.1% and the Fe⁰ decreases to 12.1%. Importantly, the amount of Fe⁰ after the application of –10 V has increased by 148% for the templated film, whereas the increase is less (47%) in the non-templated film. Unlike the non-templated film, the application of +10 V only partially reverses the reduction caused by the negative voltage in the templated film. This is again consistent with the magnetic data shown in **Figure 4b**. The application of –10 V causes partial reduction of Fe, resulting in an increase in magnetic moment at saturation. The subsequent application of +10 V only partially re-oxidizes Fe, causing a decrease in the magnetic moment at saturation, but it remains higher than in the initial state. Thus, the XPS data shown in **Figure 5** is in good agreement with the magnetic hysteresis loops and the observed change in oxidation state of Fe indicates a magneto-ionic mechanism.

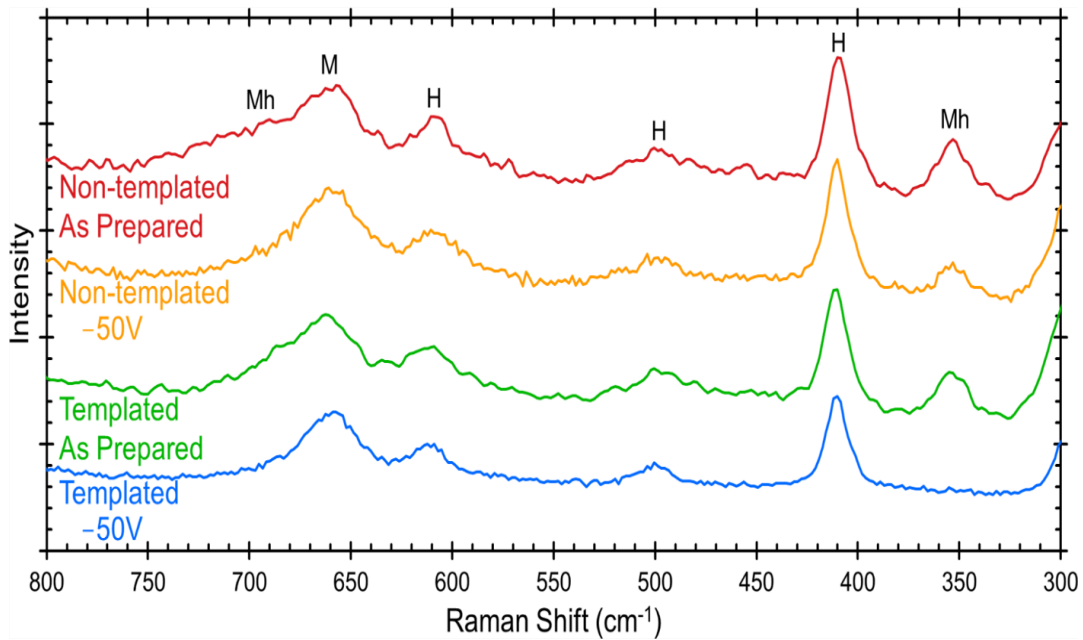


Figure 6. Raman spectra of the non-templated and templated films in the initial states and after applying -50 V. The bands from hematite are labeled with **H**, magnetite with **M**, and maghemite with **Mh**.

The crystal structure of iron oxide largely influences its magnetic properties as well. The two most common structures for iron oxide are hematite [α - Fe_2O_3] and magnetite [Fe_3O_4]. Hematite should be completely antiferromagnetic (although a small ferromagnetic-like signal, due to a canted antiferromagnetic spin structure, can be observed for α - Fe_2O_3 above the Morin transition) while magnetite, on the other hand, is ferrimagnetic. X-Ray Diffraction (XRD) is a commonly used technique to analyze the crystal structure of materials, but all of the peaks for hematite and magnetite overlap so that these phases cannot be easily distinguished by XRD. Therefore, we used Raman spectroscopy to determine the crystallographic structure of our films. **Figure 6** shows Raman spectra collected for both the non-templated and templated films in the initial states and after the application of -50 V, where the maximum change in magnetic moment at saturation was obtained. Spectra at different places on each film were taken and the results were found to be independent of location, indicating that the samples were homogeneous. The Raman bands of the various phases of iron oxide are well known and documented in the literature.^{46,60,61} The bands at 135, 150, and 260 cm^{-1} are caused by the substrate itself. The bands at 226, 245, 293, 298, 412, 500 and 612 cm^{-1} are from hematite and

the band at 660 cm^{-1} is from magnetite. The broadening of the magnetite peak at around 660 cm^{-1} could be due to the contribution of FeO (wüstite, antiferromagnetic), which has a band at *ca.* 652 cm^{-1} .⁶² There is a weak band at 690 cm^{-1} which looks like a shoulder of the magnetite band which is due to maghemite [$\gamma\text{-Fe}_2\text{O}_3$] and the band at 355 cm^{-1} is also maghemite. It is worth mentioning that pure metallic Fe does not exhibit a Raman scattering. From these data, it is not possible to precisely quantify the fraction of each phase present in the films, but relative changes can be qualitatively described since the integrated area under a band is directly proportional to the volume of material that vibrates in that mode.

In the as-prepared non-templated film, all these three phases are present, with no indication of additional iron oxide phases. After the application of -50 V , the relative intensity of both maghemite peaks (355 and 690 cm^{-1}) decreases. Concurrently, the amount of Fe_3O_4 relative to Fe_2O_3 (hematite + maghemite) increases. This is consistent with the hypothesis of oxygen anions migrating out of the nanoporous layer during negative voltage application, that is, causing an overall decrease of the O/Fe ratio in the oxide films, which is further assisted by the formation of metallic Fe (as evidenced by XPS). In the templated film, the effects of voltage are exacerbated. The as-prepared templated film is again a mixture of the three phases. After the application of -50 V , the maghemite peaks again decrease (note that the band centered at 350 cm^{-1} nearly vanishes) and the amount of magnetite relative to the amount of Fe_2O_3 phases increases, just as in the non-templated film. This suggests that, during the application of negative voltages, the maghemite phase might be partially reduced to magnetite, besides the formation of Fe^0 , to compensate the loss of oxygen which, most likely, migrates towards the outer surface of the material (towards the positive charges at the electric double layer surrounding the FeO_x).^{35,63,64} While reaching the interface, there are two possible ways for O^{2-} to be distributed: (i) to form FeO, an oxide with the highest O/Fe ratio, or (ii) outward migrate to the electrolyte. The former would go against the XPS data, where a decrease in Fe^{2+}

contribution is obtained upon application of the negative voltage (**Table 1**). In turn, it is unlikely that under negative voltage FeO forms at the bottom of FeO_x nanoporous layer (i.e., at the substrate/film interface), as O²⁻ ions should be repulsed due to Coulomb interaction. Instead, it could be suggested that the oxide ions, O²⁻, going out of the sample become stabilized by the PC molecules by solvation. As some traces of Na⁺ are present in the electrolyte, the O²⁻ species would be surrounded by the Na⁺ cations while remaining in ionized form.⁶⁵ Potential migration of these O²⁻ species toward the positively polarized Pt electrode to undergo oxidation could occur⁶³, but the fact that the process could not be reversed upon positive voltages suggest that, once stabilized by the PC, the O²⁻ species remain in the electrolyte, as illustrated in Figure 7.

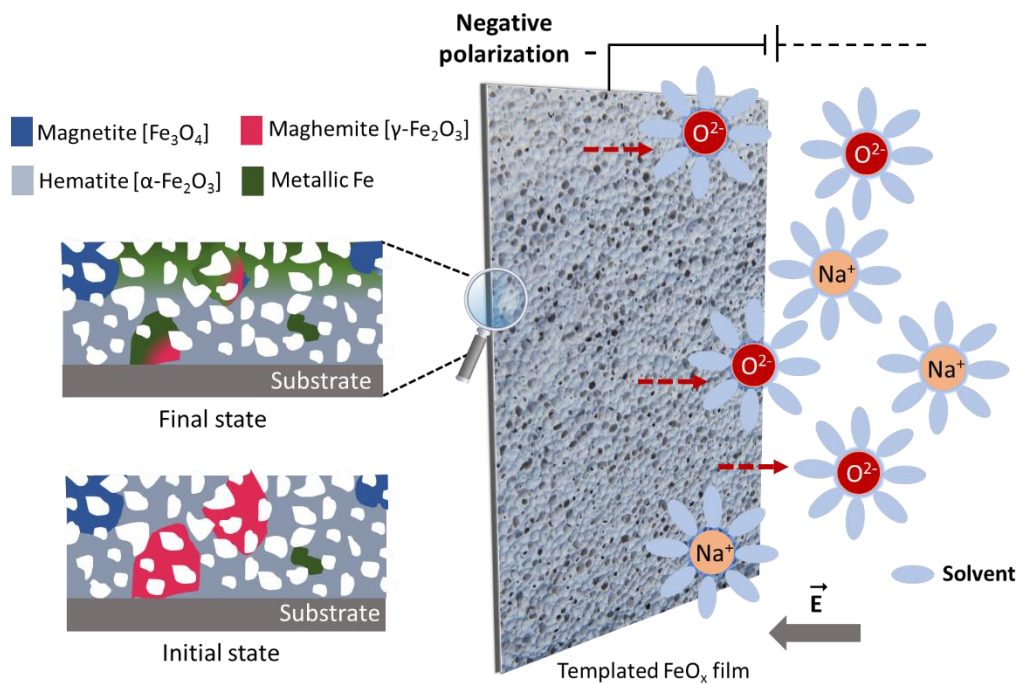


Figure 7. Illustration of magneto-ionic effect in the porous FeO_x films subject to negative voltage polarity.

The conversion of hematite/maghemite to magnetite (besides the formation of metallic Fe) further supports the observed increase of the saturation magnetization after negative voltages are applied and corroborates a magneto-ionic underlying mechanism. Indeed, the

saturation magnetization of bulk γ -Fe₂O₃ (76 emu/g)⁶⁶ is lower than for Fe₃O₄ (92 emu/g).⁶⁷ As discussed in the introduction, hematite has a hexagonal crystal structure, all of the Fe atoms are Fe³⁺, and it is antiferromagnetic. Magnetite, on the other hand, has a cubic crystal structure, comprises a mixture of Fe³⁺ and Fe²⁺ cations and is ferrimagnetic. Maghemite has a cubic crystal structure like magnetite, but all of the Fe is Fe³⁺, like in hematite. Note that this interpretation is consistent with the larger decrease of the Fe³⁺ contribution (compared to that of Fe²⁺) observed in the XPS data, particularly for the highly porous templated sample (**Table 1**). The fact that magneto-ionic effects induce crystallographic phase transformations in the porous oxide films may be partly the reason why the changes in magnetism are not entirely reversible in the templated sample, and only reversible in the non-templated sample in the ± 10 V potential window.

CONCLUSIONS

Our work demonstrates the possibility to manipulate the magnetic properties of porous iron oxide films, to a large extent, by means of electric field applied using an anhydrous electrolyte liquid media. Non-templated films (with some porosity) and block-copolymer templated films (with a larger porosity degree) were prepared by sol-gel methods. The non-templated films demonstrated a maximum increase in magnetic moment at saturation of 395% after the application of -50 V whereas the templated films showed a maximum increase of 1310% at the same voltage, underscoring the importance of porosity in promoting the magnetoelectric response. The magnetic changes in the non-templated films induced at -10 V were found to be completely reversible after the application of $+10$ V. However, the changes in the porous films induced at -10 V were only partially reversible upon applying positive voltages. This shows that there is a trade-off between high porosity leading to high magnetoelectric response and more moderate porosity, allowing reversibility in the system. XPS and Raman results show that the films are a mixture of iron oxide phases and that the

applied electric field causes phase transformations that involve changes in the Fe oxidation states. Finally, the results presented here suggest that the primary mechanism is oxygen migration both through the film (magneto-ionic effect) and exchanged between the film and the liquid electrolyte.

AUTHOR CONTRIBUTIONS

The manuscript was written through contributions of all authors. All authors have given approval to the final version of the manuscript.

NOTES

The authors declare no competing interests.

ACKNOWLEDGMENTS

This work was supported by the European Research Council under the SPIN-PORICS 2014-Consolidator Grant, Agreement № 648454, the Generalitat de Catalunya (2017-SGR-292), the Spanish Government (MAT2017-86357-C3-1-R and associated FEDER), the European Union's Horizon 2020 research and innovation programme under the Marie Skłodowska-Curie grant agreement № 665919 and the French National Research Agency (ANR) grant agreement № ANR-15-CE24-0015-01.

REFERENCES

- (1) Almasi, H.; Xu, M.; Xu, Y.; Newhouse-Illige, T.; Wang, W. G. Effect of Mo Insertion Layers on the Magnetoresistance and Perpendicular Magnetic Anisotropy in Ta/CoFeB/MgO Junctions. *Appl. Phys. Lett.* **2016**, *109* (3), 32401. <https://doi.org/10.1063/1.4958732>.

- (2) Wang, K. L.; Alzate, J. G.; Khalili Amiri, P. Low-Power Non-Volatile Spintronic Memory: STT-RAM and beyond. *J. Phys. D. Appl. Phys.* **2013**, *46* (8), 74003. <https://doi.org/10.1088/0022-3727/46/7/074003>.
- (3) Alzate, J. G.; Amiri, P. K.; Upadhyaya, P.; Cherepov, S. S.; Zhu, J.; Lewis, M.; Dorrance, R.; Katine, J. A.; Langer, J.; Galatsis, K.; et al. Voltage-Induced Switching of Nanoscale Magnetic Tunnel Junctions. *Tech. Dig. - Int. Electron Devices Meet. IEDM* **2012**, 681–684. <https://doi.org/10.1109/IEDM.2012.6479130>.
- (4) Chang, T. C.; Jian, F. Y.; Chen, S. C.; Tsai, Y. T. Developments in Nanocrystal Memory. *Mater. Today* **2011**, *14* (12), 608–615. [https://doi.org/10.1016/S1369-7021\(11\)70302-9](https://doi.org/10.1016/S1369-7021(11)70302-9).
- (5) Li, G. J.; Leung, C. W.; Lei, Z. Q.; Lin, K. W.; Lai, P. T.; Pong, P. W. T. Patterning of FePt for Magnetic Recording. *Thin Solid Films* **2011**, *519* (23), 8307–8311. <https://doi.org/10.1016/j.tsf.2011.03.088>.
- (6) Scott, J. F. Data Storage: Multiferroic Memories. *Nat. Mater.* **2007**, *6* (4), 256–257. <https://doi.org/10.1038/nmat1868>.
- (7) Moser, A.; Kentaro, T.; David, T. M.; Manfred, A.; Yoshiaki, S.; Yoshihiro, I.; Shouheng, S.; Eric, E. F. Magnetic Recording: Advancing into the Future. *J. Phys. D. Appl. Phys.* **2002**, *35* (19), R157.
- (8) Dong, C.; Jiang, C.; Wei, W.; Wu, L.; Yao, J. The Resistive Switching Memory of CoFe₂O₄ Thin Film Using Nanoporous Alumina Template. *Nanoscale Res. Lett.* **2014**, *9* (1), 584. <https://doi.org/10.1186/1556-276x-9-584>.
- (9) Srinivasan, S. Y.; Paknikar, K. M.; Bodas, D.; Gajbhiye, V. Applications of Cobalt Ferrite Nanoparticles in Biomedical Nanotechnology. *Nanomedicine* **2018**, *13* (10),

- 1221–1238. <https://doi.org/10.2217/nmm-2017-0379>.
- (10) Zang, D.; Yi, H.; Gu, Z.; Chen, L.; Han, D.; Guo, X.; Wang, S.; Liu, M.; Jiang, L. Interfacial Engineering of Hierarchically Porous NiTi/Hydrogels Nanocomposites with Exceptional Antibiofouling Surfaces. *Adv. Mater.* **2017**, *29* (2), 1602869. <https://doi.org/10.1002/adma.201602869>.
- (11) Iqbal, M. Z.; Ma, X.; Chen, T.; Zhang, L.; Ren, W.; Xiang, L.; Wu, A. Silica-Coated Super-Paramagnetic Iron Oxide Nanoparticles (SPIONPs): A New Type Contrast Agent of T 1 Magnetic Resonance Imaging (MRI). *J. Mater. Chem. B* **2015**, *3* (26), 5172–5181. <https://doi.org/10.1039/c5tb00300h>.
- (12) Sanpo, N.; Berndt, C. C.; Wen, C.; Wang, J. Transition Metal-Substituted Cobalt Ferrite Nanoparticles for Biomedical Applications. *Acta Biomater.* **2013**, *9* (3), 5830–5837. <https://doi.org/10.1016/j.actbio.2012.10.037>.
- (13) Rui, H.; Xing, R.; Xu, Z.; Hou, Y.; Goo, S.; Sun, S. Synthesis, Functionalization, and Biomedical Applications of Multifunctional Magnetic Nanoparticles. *Adv. Mater.* **2010**, *22* (25), 2729–2742. <https://doi.org/10.1002/adma.201000260>.
- (14) Berensmeier, S. Magnetic Particles for the Separation and Purification of Nucleic Acids. *Appl. Microbiol. Biotechnol.* **2006**, *73* (3), 495–504. <https://doi.org/10.1007/s00253-006-0675-0>.
- (15) Aihara, H.; Zider, J.; Fanton, G.; Duerig, T. Combustion Synthesis Porous Nitinol for Biomedical Applications. *Int. J. Biomater.* **2019**, 4307461. <https://doi.org/10.1155/2019/4307461>.
- (16) Elrefai, A. L.; Yoshida, T.; Enpuku, K. Magnetic Parameters Evaluation of Magnetic Nanoparticles for Use in Biomedical Applications. *J. Magn. Magn. Mater.* **2019**, 474,

- 522–527. <https://doi.org/10.1016/j.jmmm.2018.11.022>.
- (17) Wang, K. L.; Kou, X.; Upadhyaya, P.; Fan, Y.; Shao, Q.; Yu, G.; Amiri, P. K. Electric-Field Control of Spin-Orbit Interaction for Low-Power Spintronics. *Proc. IEEE* **2016**, *104* (10), 1974–2008. <https://doi.org/10.1109/JPROC.2016.2573836>.
- (18) Song, C.; Cui, B.; Li, F.; Zhou, X.; Pan, F. Recent Progress in Voltage Control of Magnetism: Materials, Mechanisms, and Performance. *Prog. Mater. Sci.* **2017**, *87*, 33–82. <https://doi.org/10.1016/j.pmatsci.2017.02.002>.
- (19) Udalov, O. G.; Chtchelkatchev, N. M.; Beloborodov, I. S. Electric Field Control of Magnetic Properties and Magneto-Transport in Composite Multiferroics. *J. Phys. Condens. Matter* **2015**, *27* (18), 186001. <https://doi.org/10.1088/0953-8984/27/18/186001>.
- (20) Cherifi, R. O.; Ivanovskaya, V.; Phillips, L. C.; Zobelli, A.; Infante, I. C.; Jacquet, E.; Garcia, V.; Fusil, S.; Briddon, P. R.; Guiblin, N.; et al. Electric-Field Control of Magnetic Order above Room Temperature. *Nat. Mater.* **2014**, *13* (4), 345–351. <https://doi.org/10.1038/nmat3870>.
- (21) Kim, H. K. D.; Schelhas, L. T.; Keller, S.; Hockel, J. L.; Tolbert, S. H.; Carman, G. P. Magnetoelectric Control of Superparamagnetism. *Nano Lett.* **2013**, *13* (3), 884–888. <https://doi.org/10.1021/nl3034637>.
- (22) Sun, N. X.; Srinivasan, G. Voltage Control of Magnetism in Multiferroic Heterostructures and Devices. *Spin* **2012**, *2* (3), 1240004. <https://doi.org/10.1142/s2010324712400048>.
- (23) Bonell, F.; Murakami, S.; Shiota, Y.; Nozaki, T.; Shinjo, T.; Suzuki, Y. Large Change in Perpendicular Magnetic Anisotropy Induced by an Electric Field in FePd Ultrathin

- Films. *Appl. Phys. Lett.* **2011**, 98 (23), 232510. <https://doi.org/10.1063/1.3599492>.
- (24) Zhu, X.; Zhou, J.; Chen, L.; Guo, S.; Liu, G.; Li, R.-W.; Lu, W. D. In Situ Nanoscale Electric Field Control of Magnetism by Nanoionics. *Adv. Mater.* **2016**, 28 (35), 7658–7665. <https://doi.org/10.1002/adma.201601425>.
- (25) Dasgupta, S.; Das, B.; Knapp, M.; Brand, R. A.; Ehrenberg, H.; Kruk, R.; Hahn, H. Intercalation-Driven Reversible Control of Magnetism in Bulk Ferromagnets. *Adv. Mater.* **2014**, 26 (27), 4639–4644. <https://doi.org/10.1002/adma.201305932>.
- (26) Dubraja, L. A.; Reitz, C.; Velasco, L.; Witte, R.; Kruk, R.; Hahn, H.; Brezesinski, T. Electrochemical Tuning of Magnetism in Ordered Mesoporous Transition-Metal Ferrite Films for Micromagnetic Actuation. *ACS Appl. Nano Mater.* **2018**, 1 (1), 65–72. <https://doi.org/10.1021/acsanm.7b00037>.
- (27) Reitz, C.; Wang, D.; Stoeckel, D.; Beck, A.; Leichtweiss, T.; Hahn, H.; Brezesinski, T. Applying Capacitive Energy Storage for in Situ Manipulation of Magnetization in Ordered Mesoporous Perovskite-Type LSMO Thin Films. *ACS Appl. Mater. Interfaces* **2017**, 9 (27), 22799–22807. <https://doi.org/10.1021/acsami.7b01978>.
- (28) Ueno, K.; Shimotani, H.; Iwasa, Y.; Kawasaki, M. Electrostatic Charge Accumulation versus Electrochemical Doping in SrTiO₃ Electric Double Layer Transistors. *Appl. Phys. Lett.* **2010**, 96 (25), 2008–2011. <https://doi.org/10.1063/1.3457785>.
- (29) Molinari, A.; Hahn, H.; Kruk, R. Voltage-Control of Magnetism in All-Solid-State and Solid/Liquid Magnetoelectric Composites. *Adv. Mater.* **2019**, 1806662. <https://doi.org/10.1002/adma.201806662>.
- (30) Navarro-Senent, C.; Quintana, A.; Menéndez, E.; Pellicer, E.; Sort, J. Electrolyte-Gated Magnetoelectric Actuation: Phenomenology, Materials, Mechanisms, and Prospective

- Applications. *APL Mater.* **2019**, 7 (3), 030701. <https://doi.org/10.1063/1.5080284>.
- (31) Tan, A. J.; Huang, M.; Avci, C. O.; Büttner, F.; Mann, M.; Hu, W.; Mazzoli, C.; Wilkins, S.; Tuller, H. L.; Beach, G. S. D. Magneto-Ionic Control of Magnetism Using a Solid-State Proton Pump. *Nat. Mater.* **2019**, 18 (1), 35–41. <https://doi.org/10.1038/s41563-018-0211-5>.
- (32) Baldrati, L.; Tan, A. J.; Mann, M.; Bertacco, R.; Beach, G. S. D. Magneto-Ionic Effect in CoFeB Thin Films with in-Plane and Perpendicular-to-Plane Magnetic Anisotropy. *Appl. Phys. Lett.* **2017**, 110 (1), 012404. <https://doi.org/10.1063/1.4973475>.
- (33) Gilbert, D. A.; Grutter, A. J.; Arenholz, E.; Liu, K.; Kirby, B. J.; Borchers, J. A.; Maranville, B. B. Structural and Magnetic Depth Profiles of Magneto-Ionic Heterostructures beyond the Interface Limit. *Nat. Commun.* **2016**, 7, 12264. <https://doi.org/10.1038/ncomms12264>.
- (34) Gilbert, D. A.; Olamit, J.; Dumas, R. K.; Kirby, B. J.; Grutter, A. J.; Maranville, B. B.; Arenholz, E.; Borchers, J. A.; Liu, K. Controllable Positive Exchange Bias via Redox-Driven Oxygen Migration. *Nat. Commun.* **2016**, 7, 11050. <https://doi.org/10.1038/ncomms11050>.
- (35) Bauer, U.; Yao, L.; Tan, A. J.; Agrawal, P.; Emori, S.; Tuller, H. L.; Van Dijken, S.; Beach, G. S. D. Magneto-Ionic Control of Interfacial Magnetism. *Nat. Mater.* **2015**, 14 (2), 174–181. <https://doi.org/10.1038/nmat4134>.
- (36) Bi, C.; Liu, Y.; Newhouse-Illige, T.; Xu, M.; Rosales, M.; Freeland, J. W.; Mryasov, O.; Zhang, S.; Te Velthuis, S. G. E.; Wang, W. G. Reversible Control of Co Magnetism by Voltage-Induced Oxidation. *Phys. Rev. Lett.* **2014**, 113 (26), 267202. <https://doi.org/10.1103/PhysRevLett.113.267202>.

- (37) Duschek, K.; Petr, A.; Zehner, J.; Nielsch, K.; Leistner, K. All-Electrochemical Voltage-Control of Magnetization in Metal Oxide/metal Nanoislands. *J. Mater. Chem. C* **2018**, *6* (31), 8411–8417. <https://doi.org/10.1039/c8tc01994k>.
- (38) Quintana, A.; Menéndez, E.; Liedke, M. O.; Butterling, M.; Wagner, A.; Sireus, V.; Torruella, P.; Estradé, S.; Peiró, F.; Dendooven, J.; et al. Voltage-Controlled ON-OFF Ferromagnetism at Room Temperature in a Single Metal Oxide Film. *ACS Nano* **2018**, *12*, 10291–10300. <https://doi.org/10.1021/acsnano.8b05407>.
- (39) Robbenolt, S.; Quintana, A.; Pellicer, E.; Sort, J. Large Magnetoelectric Effects Mediated by Electric-Field-Driven Nanoscale Phase Transformations in Sputtered (Nanoparticulate) and Electrochemically Dealloyed (Nanoporous) Fe-Cu Films. *Nanoscale* **2018**, *10* (30), 14570–14578. <https://doi.org/10.1039/c8nr03924k>.
- (40) Quintana, A.; Menéndez, E.; Isarain-Chávez, E.; Fornell, J.; Solsona, P.; Fauth, F.; Baró, M. D.; Nogués, J.; Pellicer, E.; Sort, J. Tunable Magnetism in Nanoporous CuNi Alloys by Reversible Voltage-Driven Element-Selective Redox Processes. *Small* **2018**, *14*, 1704396. <https://doi.org/10.1002/sml.201704396>.
- (41) Quintana, A.; Zhang, J.; Isarain-Chávez, E.; Menéndez, E.; Cuadrado, R.; Robles, R.; Baró, M. D.; Guerrero, M.; Pané, S.; Nelson, B. J.; et al. Voltage-Induced Coercivity Reduction in Nanoporous Alloy Films: A Boost toward Energy-Efficient Magnetic Actuation. *Adv. Funct. Mater.* **2017**, *27*, 1701904. <https://doi.org/10.1002/adfm.201701904>.
- (42) Chien, D.; Buditama, A. N.; Schelhas, L. T.; Kang, H. Y.; Robbenolt, S.; Chang, J. P.; Tolbert, S. H. Tuning Magnetoelectric Coupling Using Porosity in Multiferroic Nanocomposites of ALD-Grown Pb(Zr,Ti)O₃ and Templated Mesoporous CoFe₂O₄. *Appl. Phys. Lett.* **2016**, *109*, 112904. <https://doi.org/10.1063/1.4962536>.

- (43) Quickel, T. E.; Schelhas, L. T.; Farrell, R. A.; Petkov, N.; Le, V. H.; Tolbert, S. H. Mesoporous Bismuth Ferrite with Amplified Magnetoelectric Coupling and Electric Field-Induced Ferrimagnetism. *Nat. Commun.* **2015**, *6*, 6562. <https://doi.org/10.1038/ncomms7562>.
- (44) Reitz, C.; Leufke, P. M.; Schneider, R.; Hahn, H.; Brezesinski, T. Large Magnetoresistance and Electrostatic Control of Magnetism in Ordered Mesoporous $\text{La}_{1-x}\text{Ca}_x\text{MnO}_3$ Thin Films. *Chem. Mater.* **2014**, *26* (19), 5745–5751. <https://doi.org/10.1021/cm5028282>.
- (45) Petrov, V. M.; Srinivasan, G.; Laletsin, U.; Bichurin, M. I.; Tuskov, D. S.; Paddubnaya, N. Magnetoelectric Effects in Porous Ferromagnetic-Piezoelectric Bulk Composites: Experiment and Theory. *Phys. Rev. B - Condens. Matter Mater. Phys.* **2007**, *75* (17), 174422. <https://doi.org/10.1103/PhysRevB.75.174422>.
- (46) McCarty, K. F.; Monti, M.; Nie, S.; Siegel, D. A.; Starodub, E.; El Gabaly, F.; McDaniel, A. H.; Shavorskiy, A.; Tyliszczak, T.; Bluhm, H.; et al. Oxidation of magnetite(100) to Hematite Observed by in Situ Spectroscopy and Microscopy. *J. Phys. Chem. C* **2014**, *118* (34), 19768–19777. <https://doi.org/10.1021/jp5037603>.
- (47) Gaviría, J. P.; Bohé, A.; Pasquevich, A.; Pasquevich, D. M. Hematite to Magnetite Reduction Monitored by Mössbauer Spectroscopy and X-Ray Diffraction. *Phys. B Condens. Matter* **2007**, *389* (1), 198–201. <https://doi.org/10.1016/j.physb.2006.07.056>.
- (48) Gich, M.; Frontera, C.; Roig, A.; Fontcuberta, J.; Molins, E.; Bellido, N.; Simon, C.; Fleta, C. Magnetoelectric Coupling in $\epsilon\text{-Fe}_2\text{O}_3$ Nanoparticles. *Nanotechnology* **2006**, *17* (3), 687–691. <https://doi.org/10.1088/0957-4484/17/3/012>.
- (49) Feng, J. S. Y.; Pashley, R. D.; Nicolet, M. A. Magnetoelectric Properties of Magnetite Thin Films. *J. Phys. C Solid State Phys.* **1975**, *8* (7), 1010–1022.

<https://doi.org/10.1088/0022-3719/8/7/017>.

- (50) Duschek, K.; Pohl, D.; Fähler, S.; Nielsch, K.; Leistner, K. Research Update: Magnetoionic Control of Magnetization and Anisotropy in Layered Oxide/metal Heterostructures. *APL Mater.* **2016**, *4* (3), 32301. <https://doi.org/10.1063/1.4942636>.
- (51) Zhang, Q.; Luo, X.; Wang, L.; Zhang, L.; Khalid, B.; Gong, J.; Wu, H. Lithium-Ion Battery Cycling for Magnetism Control. *Nano Lett.* **2016**, *16* (1), 583–587. <https://doi.org/10.1021/acs.nanolett.5b04276>.
- (52) Traußnig, T.; Topolovec, S.; Nadeem, K.; Vinga Szabó, D.; Krenn, H.; Würschum, R. Magnetization of Fe-Oxide Based Nanocomposite Tuned by Surface Charging. *Phys. Status Solidi - Rapid Res. Lett.* **2011**, *5* (4), 150–152. <https://doi.org/10.1002/pssr.201004483>.
- (53) Gich, M.; Fina, I.; Morelli, A.; Sánchez, F.; Alexe, M.; Gàzquez, J.; Fontcuberta, J.; Roig, A. Multiferroic Iron Oxide Thin Films at Room Temperature. *Adv. Mater.* **2014**, *26* (27), 4645–4652. <https://doi.org/10.1002/adma.201400990>.
- (54) Zhang, L.; Hou, W.; Dong, G.; Zhou, Z.; Zhao, S.; Hu, Z.; Ren, W.; Chen, M.; Nan, C. W.; Ma, J.; et al. Low Voltage Induced Reversible Magnetoelectric Coupling in Fe₃O₄ Thin Films for Voltage Tunable Spintronic Devices. *Mater. Horizons* **2018**, *5* (5), 991–999. <https://doi.org/10.1039/c8mh00763b>.
- (55) Zehner, J.; Huhnstock, R.; Oswald, S.; Wolff, U.; Soldatov, I.; Ehresmann, A.; Nielsch, K.; Holzinger, D.; Leistner, K. Nonvolatile Electric Control of Exchange Bias by a Redox Transformation of the Ferromagnetic Layer. *Adv. Electron. Mater.* **2019**, *1900296*, 1900296. <https://doi.org/10.1002/aelm.201900296>.
- (56) Quickel, T. E.; Le, V. H.; Brezesinski, T.; Tolbert, S. H. On the Correlation between

- Nanoscale Structure and Magnetic Properties in Ordered Mesoporous Cobalt Ferrite (CoFe₂O₄) Thin Films. *Nano Lett.* **2010**, *10* (8), 2982–2988. <https://doi.org/10.1021/nl1014266>.
- (57) Biesinger, M. C.; Payne, B. P.; Grosvenor, A. P.; Lau, L. W. M.; Gerson, A. R.; Smart, R. S. C. Resolving Surface Chemical States in XPS Analysis of First Row Transition Metals, Oxides and Hydroxides: Cr, Mn, Fe, Co and Ni. *Appl. Surf. Sci.* **2011**, *257* (7), 2717–2730. <https://doi.org/10.1016/j.apsusc.2010.10.051>.
- (58) Tan, B. J.; Klabunde, K. J.; Sherwood, P. M. A. X-Ray Photoelectron Spectroscopy Studies of Solvated Metal Atom Dispersed Catalysts. Monometallic Iron and Bimetallic Iron-Cobalt Particles on Alumina. *Chem. Mater.* **1990**, *2* (2), 186–191. <https://doi.org/10.1021/cm00008a021>.
- (59) Capsoni, D.; Bini, M.; Ferrari, S.; Quartarone, E.; Mustarelli, P. Recent Advances in the Development of Li-Air Batteries. *J. Power Sources* **2012**, *220*, 253–263. <https://doi.org/10.1016/j.jpowsour.2012.07.123>.
- (60) Chernyshova, I. V.; Hochella, M. F.; Madden, A. S. Size-Dependent Structural Transformations of Hematite Nanoparticles. 1. Phase Transition. *Phys. Chem. Chem. Phys.* **2007**, *9* (14), 1736–1750. <https://doi.org/10.1039/b618790k>.
- (61) Chamritski, I.; Burns, G. Infrared- And Raman-Active Phonons of Magnetite, Maghemite, and Hematite: A Computer Simulation and Spectroscopic Study. *J. Phys. Chem. B* **2005**, *109* (11), 4965–4968. <https://doi.org/10.1021/jp048748h>.
- (62) Faria, D. L. A.; Venâncio Silva, S.; de Oliveira, M. T. Raman Microspectroscopy of Some Iron Oxides and Oxyhydroxides. *J. Raman Spectrosc.* **1997**, *28*, 873–878. [https://doi.org/10.1002/\(sici\)1097-4555\(199711\)28:11<873::aid-jrs177>3.3.co;2-2](https://doi.org/10.1002/(sici)1097-4555(199711)28:11<873::aid-jrs177>3.3.co;2-2).

- (63) Kumar, D.; Aluguri, R.; Chand, U.; Tseng, T. Y. Metal Oxide Resistive Switching Memory: Materials, Properties and Switching Mechanisms. *Ceram. Int.* **2017**, *43* (May), S547–S556. <https://doi.org/10.1016/j.ceramint.2017.05.289>.
- (64) Yang, M. K.; Kim, G. H.; Ju, H.; Lee, J. K.; Ryu, H. C. An Analysis Of “non-Lattice” oxygen Concentration Effect on Electrical Endurance Characteristic in Resistive Switching MnO_x Thin Film. *Appl. Phys. Lett.* **2015**, *106* (5), 053504. <https://doi.org/10.1063/1.4907704>.
- (65) Greenberg, M. S.; Wied, D. M.; Popov, A. I. Spectroscopic Studies of Ionic Solvation- XV. Alkali Metal Salts in Propylene Carbonate. *Spectrochim. Acta Part A Mol. Spectrosc.* **1973**, *29* (11), 1927–1932. [https://doi.org/10.1016/0584-8539\(73\)80177-1](https://doi.org/10.1016/0584-8539(73)80177-1).
- (66) Cao, D.; Li, H.; Pan, L.; Li, J.; Wang, X.; Jing, P.; Cheng, X.; Wang, W.; Wang, J.; Liu, Q. High Saturation Magnetization of γ -Fe₂O₃ Nano-Particles by a Facile One-Step Synthesis Approach. *Sci. Rep.* **2016**, *6*, 32360. <https://doi.org/10.1038/srep32360>.
- (67) Mascolo, M. C.; Pei, Y.; Ring, T. A. Room Temperature Co-Precipitation Synthesis of Magnetite Nanoparticles in a Large Ph Window with Different Bases. *Materials (Basel)*. **2013**, *6* (12), 5549–5567. <https://doi.org/10.3390/ma6125549>.